Microporous and Mesoporous Materials 309 (2020) 110585

Contents lists available at ScienceDirect

Microporous and Mesoporous Materials

journal homepage: http://www.elsevier.com/locate/micromeso

Fabrication of Cu-CHA composites with enhanced NH_3-SCR catalytic performances and hydrothermal stabilities

Lijing Sun [a,b,1], Miao Yang [a,1], Lei Cao [a], Yi Cao [c], Shutao Xu [a], Dali Zhu [a,b], Peng Tian [a,**], Zhongmin Liu [a,*]

[a] National Engineering Laboratory for Methanol to Olefins, Dalian Institute of Chemical Physics, Chinese Academy of Sciences, Dalian, 116023, Liaoning, China
[b] University of Chinese Academy of Sciences, Beijing, 100049, China
[c] School of Material Science and Chemical Engineering, Ningbo University, Ningbo, 315211, Zhejiang, China

ARTICLE INFO

Keywords:
Cu-CHA
NH_3-SCR
Composite zeolite
Hydrothermal synthesis
Hydrothermal stability

ABSTRACT

Cu-SSZ-13 and Cu-SAPO-34, both with CHA topology but different compositions, are highly active NH_3-SCR catalysts for the abatement of harmful nitrogen oxides from the exhausts of lean-burn engines. However, the former suffers from high preparation cost and worse high-temperature hydrothermal stability, and the latter is limited by its poor low-temperature hydrothermal stability. Herein, a new Cu-CHA composite (named Cu-CHA_{DNL}) containing both microenvironments of SSZ-13 and SAPO-34 was synthesized by employing one-pot synthesized Cu-SSZ-13 as Cu source, seeds and part of Si/Al source. The resultant materials have cubic-like morphology, high Si contents, controllable Cu loadings and uniform Si/P/Al/Cu elemental distributions. Solid state MAS NMR, NH_3-DRIFTS and H_2-TPR demonstrate the coexistence of aluminosilicate and SAPO zones in the Cu-CHA_{DNL} crystals. Notably, Cu-CHA_{DNL} exhibits high NH_3-SCR activity in wide temperature window and robust resistance against both steaming at 800 °C and soaking in 80 °C water. These advantages are owing to the unique composite microstructures of Cu-CHA_{DNL} and suggest the material has huge application potential in deNO_x process.

1. Introduction

Selective catalytic reduction of NO_x by urea or ammonia (NH_3-SCR) has been proven to be the most effective and economical technology to reduce NO_x emission from diesel engine exhaust [1,2]. Cu^{2+} ions exchanged zeolites are considered to be the most promising catalyst candidates for this reaction. Especially, the development of small pore Cu-chabazite (CHA) catalysts, i.e. Cu-SSZ-13 and Cu-SAPO-34 represent a great progress in the area of NH_3-SCR which show broad NH_3-SCR active temperature windows and robust hydrothermal stabilities [3]. Nevertheless, the increasingly stringent emission standards together with the development of diesel engine technique require continuous improvement of the NH_3-SCR catalyst. An ideal NH_3-SCR catalyst needs not only a wider active temperature window to meet the complex diesel engine working conditions, but also should be able to cope with more severe aging conditions, and have a more economical preparation cost.

Cu-SSZ-13 and Cu-SAPO-34 are isostructural aluminosilicate and SAPO materials. Despite components (including P or not) seems to be the main difference between them, they have distinct preparation strategies [4,5] and acid centers generation mechanisms [6,7], resulting in diverse catalytic performances and hydrothermal stabilities [8,9]. At present, Cu-SSZ-13 still suffers from high preparation cost and insufficient hydrothermal stability at high temperature. An expensive template N, N, N-trimethyl-1-adamantammonium hydroxide (TMAdaOH) is normally required for the preparation of SSZ-13 [10]. Considerable efforts have been made to reduce the synthetic cost [11–16]. However, to tune the Si/Al of SSZ-13 without TMAdaOH remains challenging although it may improve the hydrothermal stability [17]. A low-cost copper-amine complex (Cu-TEPA) has been found to be an efficient template for the one-pot synthesis of Cu-SSZ-13 [16]. Since the Cu-TEPA plays as both template and Cu source, the product has a quite high Cu content. A reversed ion-exchange with NH_4NO_3 solution has to be employed to decrease the Cu content in order to optimize the catalytic performance [18]. In addition, the Si/Al ratio of Cu-TEPA templated Cu-SSZ-13 is still

* Corresponding author.
** Corresponding author.
E-mail addresses: tianpeng@dicp.ac.cn (P. Tian), iuzm@dicp.ac.cn (Z. Liu).
[1] These authors contributed equally to this work.

https://doi.org/10.1016/j.micromeso.2020.110585
Received 22 May 2020; Received in revised form 13 August 2020; Accepted 24 August 2020
Available online 28 August 2020

low, which is easy to dealuminate and deactivate after hydrothermal aging at high temperature. The integration of diesel particulate filters (DPF) with SCR and its frequent regeneration always exposes SCR catalysts to high temperature environment [19]. To enhance the hydrothermal stability of Cu-SSZ-13 is highly desirable to avoid dealumination and maintain its activity. Quantitative introduction of rare earth or alkali metal cations has to be tried to improve the activity and the hydrothermal stability of Cu-SSZ-13 which requires additional treatment steps [20,21].

Cu-SAPO-34, by contrast, has a lower synthetic cost, better activity at low temperature and more excellent high-temperature hydrothermal stability. Over 30 types of templates have been reported to be able to direct SAPO-34 including cheap triethylamine (TEA), diethylamine (DEA) and morpholine (MOR) [22], which is possible to manipulate the acid property (Si content and distribution) and consequently the Cu species distributions of Cu-SAPO-34 [23]. The generated Brønsted acid sites through the incorporation of Si atoms into the neutral $AlPO_4$ framework are milder than its aluminosilicate analogue [6,7] favorable for its better low temperature activity [8,24]. More importantly, the migrations of phosphorus atoms or non-framework Al and P atoms to framework vacancies [25,26] together with the movements of Cu^{2+} ions [27] are possible driven by high temperature contributing to its high stability. Unfortunately, an irreversible framework degradation will happen to SAPO-34 in certain extent during the repeatedly ion-exchange (Cu-loading) processes in aqueous solution [28] or upon exposure to low-temperature moisture atmosphere [29], which will not happen to SSZ-13 at all. Considerable efforts have also been made to solve this problem including to introduce rare earth ions like Ce^{3+} and La^{3+} during the ion-exchange process [30,31] and to develop solid-state ion--exchange (SSIE) [32] and direct ion-exchange (DIE) methods [33]. "One-pot" synthesis of Cu-SAPO-34 by using Cu-TEPA as a template and copper source has also been developed [34] to omit the Cu-loading step. Unfortunately, the Cu-TEPA tends to direct Cu-SAPO-34s with abundant Si-islands resulting in the declined catalytic performance and hydrothermal stability. It is highly desirable to develop a new strategy to prepare a Cu-CHA catalyst material with both advantages of Cu-SSZ-13 and Cu-SAPO-34. Some zeolite-zeolite composites have been synthesized through two-phase intergrowth with the aim to possess both advantages of individual zeolites and display specific synergistic properties [35,36]. But the reports on the hybrid of SSZ-13 and SAPO-34 are rare despite their similar CHA structural units may benefit the intergrowth of the two phases [37,38].

In this work, we develop a new strategy to synthesize composites of Cu-SSZ-13 and Cu-SAPO-34 with the aim to optimize the catalytic property and hydrothermal stability of Cu-CHA catalyst. The obtained materials are named Cu-CHA_{DNL} (DNL means "Dalian National Laboratory for Clean Energy"). Cu-CHA_{DNL} samples exhibit typical rhombohedral morphology of SAPO-34, but with extra-high silicon contents and uniform Si/P/Al/Cu elemental distributions. EDX mapping of the thinned Cu-CHA_{DNL} crystal section further confirms the homogeneity of the material. Solid state ^{27}Al MQ MAS NMR and NH_3-DRIFTS reveal the coexistence of both aluminosilicate and SAPO domains in Cu-CHA_{DNL}. More importantly, Cu-CHA_{DNL} exhibits extraordinary NH_3-SCR catalytic performance and robust hydrothermal stability at both high and low temperatures.

2. Materials and methods

2.1. Raw materials

The raw materials used include phosphoric acid (H_3PO_4, 85 wt%), silica sol (SiO_2, 31 wt%), pseudoboehmite (Al_2O_3, 67 wt%), sodium aluminate ($NaAlO_2$, 88 wt%), copper (II) sulfate pentahydrate ($CuSO_4{\cdot}5H_2O$, 98 wt%), tetraethylenepentamine (TEPA, 99 wt%), N,N,N-trimethyl-1-adamantammonium hydroxide (TMAdaOH, 20 wt%), triethylamine (TEA, 99 wt%), diethylamine (DEA, 99 wt%) and sodium hydroxide (NaOH, 99 wt%). All the chemicals were obtained from commercial suppliers and used directly without further purification.

2.2. Synthesis of Cu-SSZ-13 precursors

Cu-SSZ-13 was synthesized by using a modified "one-pot" procedure reported in the literatures [16,39]. 5% ball-milled SAPO-34 was introduced into the synthetic gel. TMAdaOH was introduced if necessary to enhance the Si/Al ratio of Cu-SSZ-13 [39]. The molar compositions of the final gels were 11 SiO_2/1.0 Al_2O_3/2.0 $CuSO_4{\cdot}5H_2O$/2.0 TEPA/6.0 NaOH/200H_2O and 11 SiO_2/0.3 Al_2O_3/1.1 $CuSO_4{\cdot}5H_2O$/1.1 TEPA/1.0 TMAdaOH/2.0 NaOH/175H_2O. The crystallization was carried out in Teflon-lined autoclaves at 140–160 °C for 2–4 days under rotation. The products were collected by centrifugation, washed with deionized H_2O, and dried at 100 °C for 24 h, which were named as P1-13 and P2-13, respectively.

2.3. Synthesis of Cu-CHA_{DNL}

The crystallization of Cu-CHA_{DNL} was conducted in a typical synthetic gel of SAPO-34 but with P1-13 or P2-13 as a Cu source, part of Si/Al source and seeds. Typically, pseudoboehmite was first dissolved into a certain amount of distilled water followed by the addition of phosphoric acid, silica sol, organic amine (TEA or DEA) and P1-13/P2-13. The molar compositions of the reactants were 1.0 Al_2O_3/0.9 P_2O_5/(2.7–3.0) R/(0.1–0.6) SiO_2/55H_2O (R = TEA or DEA). The amount of P1-13 or P2-13 added ranges from 14 to 32 wt% depending on the Cu content expected. The percentage was calculated based on the total weight of inorganic oxides including the precursor. The final mixture was transferred to a Teflon-lined autoclave and heated at 200 °C for 24 h under rotation. The product was collected by centrifugation, washed with deionized H_2O, and dried at 100 °C in air overnight. Before the catalytic test, the sample was calcined at 600 °C for 3 h to remove the organics.

2.4. Characterizations

The powder XRD patterns were recorded on a PANalytical X'Pert PRO X-ray diffractometer with Cu-Ka radiation ($\lambda = 1.54059$ Å) at 40 KV and 40 mA. Element analyses of the samples were tested on a Philips Magix-601 X-ray fluorescence (XRF) spectrometer. X-ray photoelectron spectroscopy (XPS) was determined by employing a Thermo ESCALAB 250Xi X-ray photoelectron spectrometer with Al Ka radiation. The peak of Al 2p at 74.7 eV from Al_2O_3 on the surface of the samples was used as the internal standard. The crystal morphology of the samples was observed by a Hitachi S–3400 N scanning electron microscopy (SEM). Energy dispersive X-ray spectroscopy (EDX) was obtained on a Hitachi SU8020 field emission scanning electron microscopy equipped with a Horiba X-max silicon drift X-ray detector. To investigate the interior of the sample, the sample was cut into 50 nm slices and loaded by nickel net. Textural properties of the calcined samples were determined by N_2 adsorption at 77 K on a Micrometrics ASAP 2020 system. The total surface area was calculated based on the Brunauer-Emmett-Teller (BET) equation, and the micropore volume and surface area were determined by using the t-plot method. Diffuse reflectance UV–Vis spectra were recorded on a VARIAN Cary-5000 UV–Vis–NIR spectrophotometer equipped with an integration sphere, and the background of the UV–Vis spectrum was against a $BaSO_4$ reference standard. The temperature-programmed desorption of ammonia (NH_3-TPD) experiments were conducted in a Micromeritics Autochem II 2920 device. 100 mg calcined sample particles (40–60 mesh) were loaded into a U-quartz tube and pretreated at 650 °C for 1 h in He flow (30 mL/min) to remove the impurities, and then treated in a gas mixture of 2% NH_3-98% He flow (30 mL/min) at 120 °C to saturate the sample surface with NH_3 adsorption (60 min). After this, He flow (30 mL/min) purged through the sample for 30 min to remove the weakly adsorbed NH_3 molecules.

Table 1
Synthesis [a] and results of Cu-CHA_{DNL}-DEA/TEA with P1-13 precursor.

Sample	XRF			XPS		Yield (%) [b]	S_{micro} ($m^2\ g^{-1}$) [c]	V_{micro} ($cm^3\ g^{-1}$) [d]
	Composition	Cu content (wt%)	Na content (wt%)	Composition	Cu content (wt%)			
P1-13	Si/Al = 4.0	11.1	1.9	–	–	87.3	313	0.15
Cu-CHA_{DNL}-DEA	$Al_{0.43}P_{0.28}Si_{0.29}O_2$	2.8	0.4	$Al_{0.42}P_{0.29}Si_{0.29}O_2$	0.9	78.7	446	0.22
Cu-CHA_{DNL}-TEA	$Al_{0.40}P_{0.30}Si_{0.30}O_2$	2.6	0.5	$Al_{0.43}P_{0.33}Si_{0.24}O_2$	0.9	82.3	464	0.23

[a] The gel composition of Cu-CHA_{DNL}-DEA is 0.9 P_2O_5/1.0 Al_2O_3/0.3 SiO_2/2.7 DEA/55H_2O with 25 wt% addition of P1-13; the gel composition of Cu-CHA_{DNL}-TEA is 0.9 P_2O_5/1.0 Al_2O_3/0.3 SiO_2/3.0 TEA/55H_2O with 25 wt% addition of P1-13 (200 °C, 24 h). The percentage is calculated based on the total weight of inorganic oxides including the precursor.
[b] Calculation based on the following equation: Solid yield = Wproduct * 85%/($W_{SiO2\ +\ P2O5\ +\ Al2O3}$ + $W_{P2\text{-}13}$ * 85%).
[c] T-plot micropore surface area.
[d] T-plot micropore volume.

The measurement of the desorbed NH_3 was performed from 100 to 600 °C (10 °C/min) under He flow (30 mL/min).

The ^{29}Si, ^{27}Al and ^{31}P MAS NMR spectra were obtained on a Bruker Avance III 600 spectrometer operated at a 14.1 T wide-bore magnet. The resonance frequencies were 119.2, 156.4 and 242.9 MHz for ^{29}Si, ^{27}Al and ^{31}P MAS NMR, respectively. The spinning rates of the samples at the magic angle for ^{29}Si, ^{27}Al and ^{31}P were 10, 12 and 12 KHz, respectively. The reference materials for the chemical shift (in ppm) determination for ^{29}Si, ^{27}Al and ^{31}P were 2,2-dimethyl-2-ilapentane-5-sulfonate sodium salt (DSS), $(NH_4)Al(SO_4)_2{\cdot}12H_2O$ and 85% H_3PO_4. Two-dimensional (2D) ^{27}Al multiple quantum magic angle spinning (MQ MAS) NMR analysis was performed on a 4 mm H-X WVT probe at a spinning rate of 13 KHz. A rf field of 49.1 KHz was used for the creation (0Q→±s u and first conversion (±3Qnd f pulses. The central transition selective soft 90° pulse used for the last conversion step (0Qlse used for thKHz. A shearing transformation was used to achieve 2D Fourier transformation and obtain a pure absorption-mode 2D contour plot. The quadrupolar interaction product, PQ (PQ is identical to the "second order quadrupole effect (SOQE)" parameter used in various publications), and isotropic chemical shift (δ_{iso}) values were calculated according to procedures reported previously [40].

Electron paramagnetic resonance (EPR) was performed on a Bruker A 200 spectrometer. The sample was sealed into a quartz tube and pretreated at 120 °C in pure N_2 flow for 12 h. During spectral collection, microwave power was 2 mW, and frequency was 9.52 GHz. The sweep width was 2000 G and sweep time was 84 s, modulated at 100 KHz with a 2 G amplitude. A time constant of 41 ms was used. The spectrum was collected at 102 K.

The temperature-programmed reduction of hydrogen (H_2-TPR) was obtained on a Micromeritics Autochem II 2920 device. 100 mg calcined sample particles (40–60 mesh) were pretreated at 500 °C for 30 min in 2% O_2/He flow (30 mL/min) to remove the impurities and then cooled down to 100 °C by purging in Ar (30 mL/min). The H_2-TPR was treated from 100 to 900 °C with a rate of 10 °C/min under a 10% H_2-90% Ar flow (30 mL/min). A TCD detector was used to detect the consumption of H_2.

Diffuse reflectance infrared Fourier transform spectroscopy (DRIFTS) was conducted on a Bruker Tensor 27 Fourier-transform infrared spectroscopy equipped with a gas cell. *Ca.* 20 mg calcined sample was loaded into the sample cup and put into the high-temperature reaction chamber. The pretreatment condition was 550 °C in N_2 flow (20 mL/min) for 1 h before cooling to 150 °C. After that, the sample was treated by pre-adsorption NH_3 in a 24 mL/min flow rate containing 830 ppm NH_3 in a balance of N_2 for 30 min. The DRIFTS were tested at 200 °C with pure N_2 flow (20 mL/min). The background spectra were recorded at 200 °C after exposing the sample to 20 mL/min pure N_2 for 30 min.

2.5. Catalyst evaluation

The NH_3-SCR reaction was tested by using 60 mg of catalyst (60–80 mesh) diluted by 240 mg of quartz beads (60–80 mesh) in a fixed bed quartz reactor. To determine the temperature of catalyst, the thermal couple was placed in the centre of catalyst bed. Before entering the reactor, the reactant gases were regulated by mass-flow controllers (Brookers). All gas lines were heated to 100 °C to prevent the condensation of vapor. The composition of the reactant gases was as follows: 500 ppm of NO, 500 ppm of NH_3, 6.1% of O_2, 6.4% of H_2O and balanced with N_2 with the flow rate of 320 mL/min. The gas hourly space velocity (GHSV) was 300,000 h^{-1}. The concentrations of NO_x (NO and NO_2) and N_2O in the inlet and outlet gases were continually analyzed by a Tensor 27, Bruker Fourier transform infrared (FTIR) spectrometer equipped with a 2 m gas cell. All catalysts were pretreated in the reactant gases at 550 °C for 2 h before activity test. Catalytic activity tests were carried out over the temperature range of 150–550 °C. And before recording the activity results, the reaction was holding at each temperature for 40min. The NO_x conversion was calculated by using the following formula:

$$NO_x\ \text{conversion} = \frac{(NO + NO_2 + N_2O)_{in} - (NO + NO_2 + N_2O)_{out}}{(NO + NO_2)_{in}} \times 100\%$$

2.6. Hydrothermal stability evaluation

After a standard NH_3-SCR evaluation, the samples were further heated to 600 °C in dry air for *ca.* 15 min in the quartz reactor. And then, a 253 mL/min gas flow of air containing 10% water passed through the sample at 800 °C for 16 h to make a high-temperature hydrothermal treatment.

For the low-temperature hydrothermal stability test, the calcined sample was immersed 80 °C deionized water for 24 h in a closed vessel, and then collected by filtration and dried at 120 °C in air.

Before any characterization or evaluation, the steam treated samples were further heated to 600 °C in dry air and then kept in oven at 120 °C.

3. Results and discussion

3.1. Synthesis and characterizations of Cu-CHA_{DNL} with P1-13 precursor

A nano-sized Cu-SSZ-13 with Si/Al ratio of 4.0 and Cu loading of 11.1 wt% (named P1-13) was first synthesized by using Cu-TEPA as a template. It was employed as a Cu source, part of Si/Al source and seeds to assist the crystallization of Cu-SAPO-34. Both organic templates of DEA and TEA were tried, and the products were designated as Cu-CHA_{DNL}-DEA and Cu-CHA_{DNL}-TEA. As displayed in Table 1, both Cu-CHA_{DNL}-DEA and Cu-CHA_{DNL}-TEA had very high Si content (*ca.* 29%). Comparatively, the Si content is about 20% for conventional Si-rich SAPO-34 [41,42]. Such high Si content of Cu-CHA_{DNL} should be

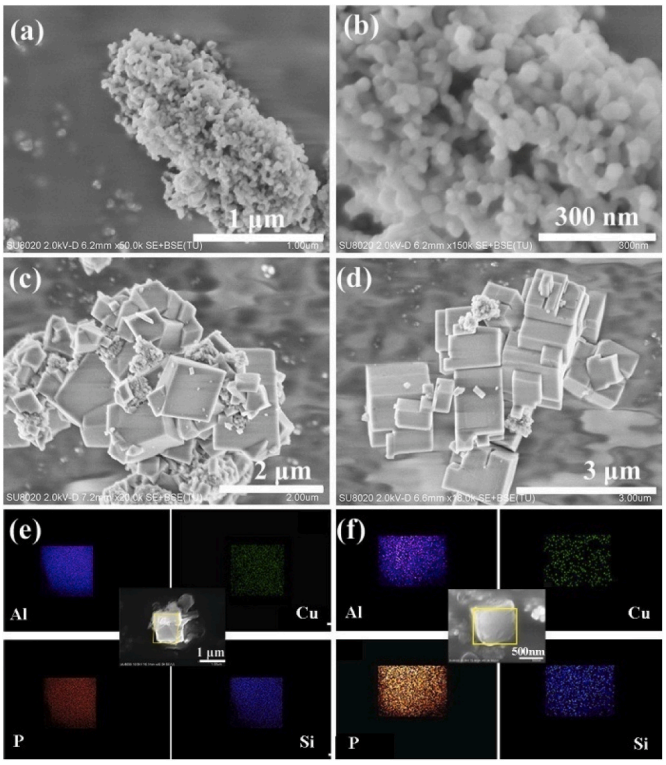

Fig. 1. SEM images of (a, b) P1-13, (c) Cu-CHA$_{DNL}$-DEA and (d) Cu-CHA$_{DNL}$-TEA. EDX maps (Al, Cu, P, Si) of (e) Cu-CHA$_{DNL}$-DEA and (f) Cu-CHA$_{DNL}$-TEA.

directly related to the introduction of P1-13 precursor with abundant silica source. Suitable Cu (2.6–2.8 wt%) and Na (0.4–0.5 wt%) loadings were also brought by P1-13 spontaneously. The XRD patterns of Cu-CHA$_{DNL}$-DEA and Cu-CHA$_{DNL}$-TEA were identical to that of P1-13 which could be indexed to the CHA phase (Fig. S1). The large half-peak width of P1-13 suggested its smaller crystal size. The SEM images of P1-13 and Cu-CHA$_{DNL}$ products are shown in Fig. 1. P1-13 presented the aggregation of small nanocrystals with particle size of *ca.* 30–50 nm (Fig. 1a and b). The product crystals showed completely different rhombohedral morphology with particle size of 1–2 μm (Fig. 1c and d). Some irregular small crystals attached on big ones could be observed for Cu-CHA$_{DNL}$-DEA, which couldn't be separated even by ultrasound. The distinct morphology between Cu-CHA$_{DNL}$ and P1-13 implies that P1-13 precursor has undergone an evolution during the crystallization of Cu-CHA$_{DNL}$.

N_2 adsorption measurements shown in Table 1 gave high micropore surface areas and micropore volumes for Cu-CHA$_{DNL}$-DEA and Cu-CHA$_{DNL}$-TEA confirming their high crystallinity. The poor textural property of P1-13 is possibly related to its high Cu loading and smaller crystal size with more defects. In addition, EDX mappings (Fig. 1e and f) demonstrated homogeneous elemental distributions of Al, Si, P and Cu in the Cu-CHA$_{DNL}$ crystals. XPS analyses showed that the crystal surface had lower Cu contents and comparable Si content with the bulk composition. Given the fact that P1-13 is the only Cu source in the syntheses, these characterizations suggest that the precursor is fully involved in the crystallization process of Cu-CHA$_{DNL}$.

3.2. NH_3-SCR performances of Cu-CHA$_{DNL}$ samples

The catalytic performances of Cu-CHA$_{DNL}$ samples in standard NH_3-SCR reaction before and after hydrothermal treatments were evaluated, and the results are given in Fig. 2. The fresh Cu-CHA$_{DNL}$-DEA exhibited close to 100% NO_x conversions from 175 to 550 °C which changed little after steam treatment at 800 °C for 16 h (red line). After immersion in 80 °C water for 24 h, the high activity of Cu-CHA$_{DNL}$-DEA was still kept well in the temperature window of 250–550 °C. Such stability was quite surprising since the treatment conditions used herein were extremely more severe than the conventional ones [29]. The situation of Cu-CHA$_{DNL}$-TEA was similar to that of Cu-CHA$_{DNL}$-DEA. It showed even better resistance to the low-temperature hydrothermal aging than Cu-CHA$_{DNL}$-DEA, though the low-temperature activities on fresh Cu-CHA$_{DNL}$-TEA and Cu-CHA$_{DNL}$-TEA-HT were relatively low. The difference of the two samples may be attributed to their different templates which lead to the difference in Si environments and acid properties of Cu-SAPO-34, [23] as revealed by the NH_3-TPD results (Fig. S2). The more acid sites on Cu-CHA$_{DNL}$-DEA than Cu-CHA$_{DNL}$-TEA are consistent with the smaller template size (higher charge density) and favors its low-temperature SCR activity. However, the higher acid density of Cu-CHA$_{DNL}$-DEA leads to a relatively low moisture stability compared with Cu-CHA$_{DNL}$-TEA. It implies that large molecule amines are better choice for the synthesis of Cu-CHA$_{DNL}$ with high moisture stability.

For comparison, one-pot synthesized Cu-SSZ-13 (R-SSZ-13, Si/Al = 9.3, 4.3 wt% Cu content), Cu-SAPO-34 (R-SAPO-34, $Al_{0.48}P_{0.35}Si_{0.17}O_2$, 3.7 wt% Cu content) and a physical mixture of Cu-SSZ-13 and Cu-SAPO-34 (R-13&34, $Al_{0.37}P_{0.25}Si_{0.38}O_2$, 3.8 wt% Cu content), were prepared to evaluate their NH_3-SCR performances. It is noted that the compositions of high silica Cu-CHA$_{DNL}$ are quite special, which can only be achieved

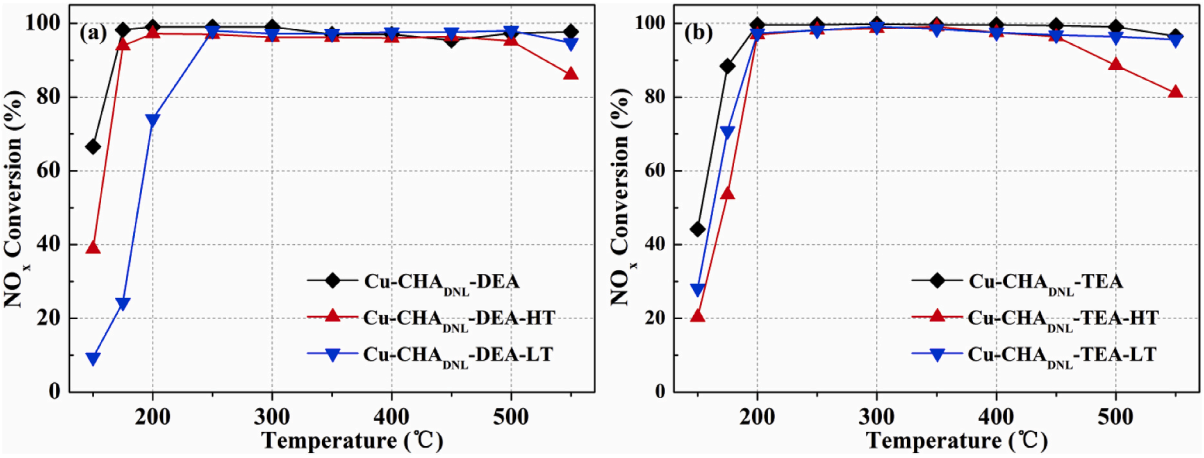

Fig. 2. NO_x conversion as a function of reaction temperature over Cu-CHA$_{DNL}$ samples. Fresh (black◆), high-temperature steam treated (HT) (red▲) and low-temperature water soaked (LT) (blue▼). The feed contains 500 ppm of NO, 500 ppm of NH_3, 6.1% of O_2, 6.4% of H_2O and balanced with N_2 at 300,000 h^{-1} gas hourly space velocity. (For interpretation of the references to color in this figure legend, the reader is referred to the Web version of this article.)

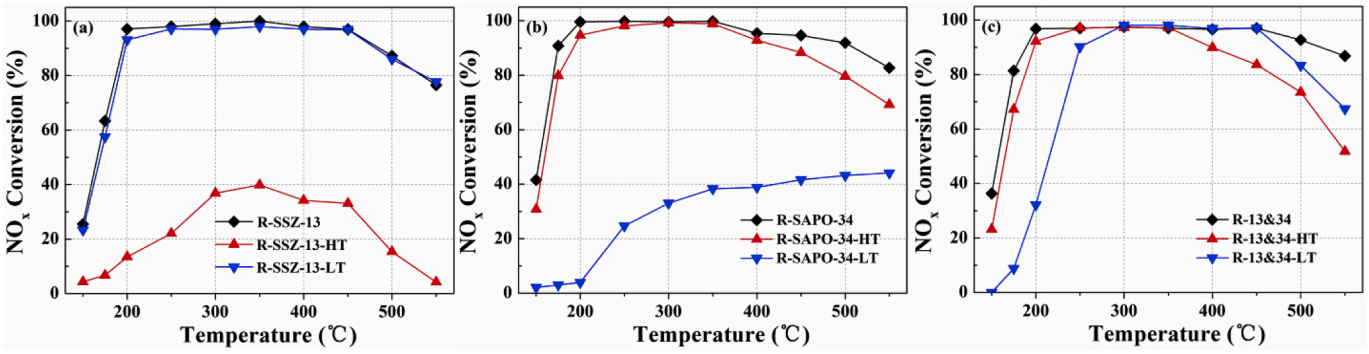

Fig. 3. NO_x conversion as a function of reaction temperature over reference samples. Fresh (black◆), high-temperature steam treated (HT) (red▲, and low-temperature water soaked (LT) (blue▼). The feed contains 500 ppm of NO, 500 ppm of NH_3, 6.1% of O_2, 6.4% of H_2O and balanced with N_2 at 300,000 h^{-1} gas hourly space velocity. (For interpretation of the references to color in this figure legend, the reader is referred to the Web version of this article.)

Table 2
Synthesis and results of Cu-CHA_{DNL}-n with P2-13 precursor.

Sample [a]	Gel		Product				
	X SiO_2	Y (wt%) [b]	Composition [c]	Cu content (wt%) [c]	Na content (wt%) [c]	Solid yield A (%) [d]	Solid yield B (%) [d]
Cu-CHA_{DNL}-1	0.1	25	$Al_{0.45}P_{0.36}Si_{0.19}O_2$	2.4	0.4	80.1	72.7
Cu-CHA_{DNL}-2	0.3	14	$Al_{0.52}P_{0.33}Si_{0.15}O_2$	1.5	0.3	72.4	67.6
Cu-CHA_{DNL}-3	0.3	25	$Al_{0.45}P_{0.35}Si_{0.20}O_2$	2.8	0.5	78.5	70.9
Cu-CHA_{DNL}-4	0.3	32	$Al_{0.40}P_{0.30}Si_{0.30}O_2$	3.1	0.6	82.0	72.5
Cu-CHA_{DNL}-5	0.6	25	$Al_{0.44}P_{0.34}Si_{0.22}O_2$	2.3	0.5	79.0	72.1
P2-13	-	-	Si/Al = 9.3	8.4	2.0	-	-

[a] The gel composition is 0.9 P_2O_5/1.0 Al_2O_3/X SiO_2/3.0 TEA/55H_2O with the addition of Y wt% P2-13 precursor (200 °C, 24 h).
[b] Precursor dosage = $W_{P2\text{-}13}$ * 85%/($W_{SiO2+P2O5+Al2O3}$ + $W_{P2\text{-}13}$ * 85%).
[c] Determined by XRF.
[d] Calculation based on the following equation: Solid yield A = $W_{product}$ * 85%/($W_{SiO2\ +\ P2O5\ +\ Al2O3}$ + $W_{P2\text{-}13}$ * 85%), Solid yield B = ($W_{product}$ - $W_{P2\text{-}13}$) * 85%/$WSiO_2$ + P_2O_5 + Al_2O_3.

by mixing Cu-SSZ-13 and Cu-SAPO-34. As shown in Fig. 3a, R-SSZ-13 presented lower NO_x conversion at both low-temperature (T < 200 °C) and high-temperature (T > 450 °C) ranges. Although R-SSZ-13-LT could survive the low-temperature hydrothermal treatment, R-SSZ-13-HT lost most NH_3-SCR activity after 800 °C steaming for 16 h, and the maximum NO_x conversion was only 39% at 350 °C. R-SAPO-34 had an inferior fresh activity than Cu-CHA_{DNL}-DEA, meanwhile it had outstanding stability against high-temperature hydrothermal treatment (Fig. 3b). As expected, it deactivated completely after immersing in 80 °C water for 24 h. The catalytic performance of R-13&34 with comparable composition to Cu-CHA_{DNL} had 100% conversion in the range of 200–450 °C (Fig. 3c). However, the temperature window of *ca.* 100% conversion shrunk to 250–350 °C after 800 °C steam aging, and 300–450 °C after 80 °C water immersion. The above results clearly confirm that Cu-CHA_{DNL} samples are different from conventional Cu-SAPO-34, Cu-SSZ-13 and their physical mixture. The former have superior NH_3-SCR activities in wide temperature window, more robust hydrothermal stabilities at both high and low temperatures. Combining its economic preparation cost, Cu-CHA_{DNL} should be very attractive for industrial applications.

3.3. *Synthesis, characterizations and NH_3-SCR performance of Cu-CHA_{DNL} with P2-13 precursor*

With the aim to further optimize the NH_3-SCR activity and stability, and to understand the crystallization process of Cu-CHA_{DNL}, P2-13 with higher Si/Al ratio of 9.3 was further synthesized with the assistance of TMAdaOH template, which was used for the crystallization of Cu-CHA_{DNL} to tune the product composition. The crystallinity of P2-13 herein was controlled to be low by shortening reaction time, in order to enhance its activity in the subsequent crystallization. Because of the introduction of TMAdaOH, two XRD peaks of P2-13 shifted from 16.1°

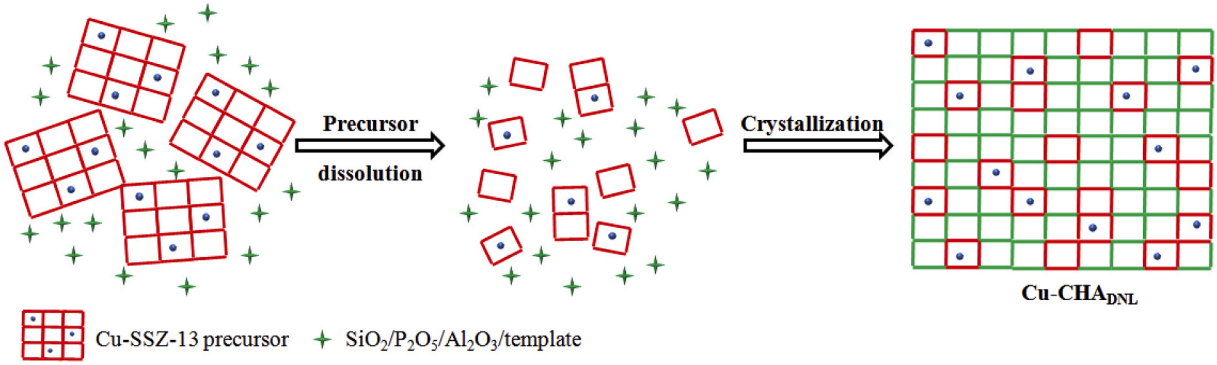

Fig. 4. Proposed crystallization process of the Cu-CHA_{DNL} sample.

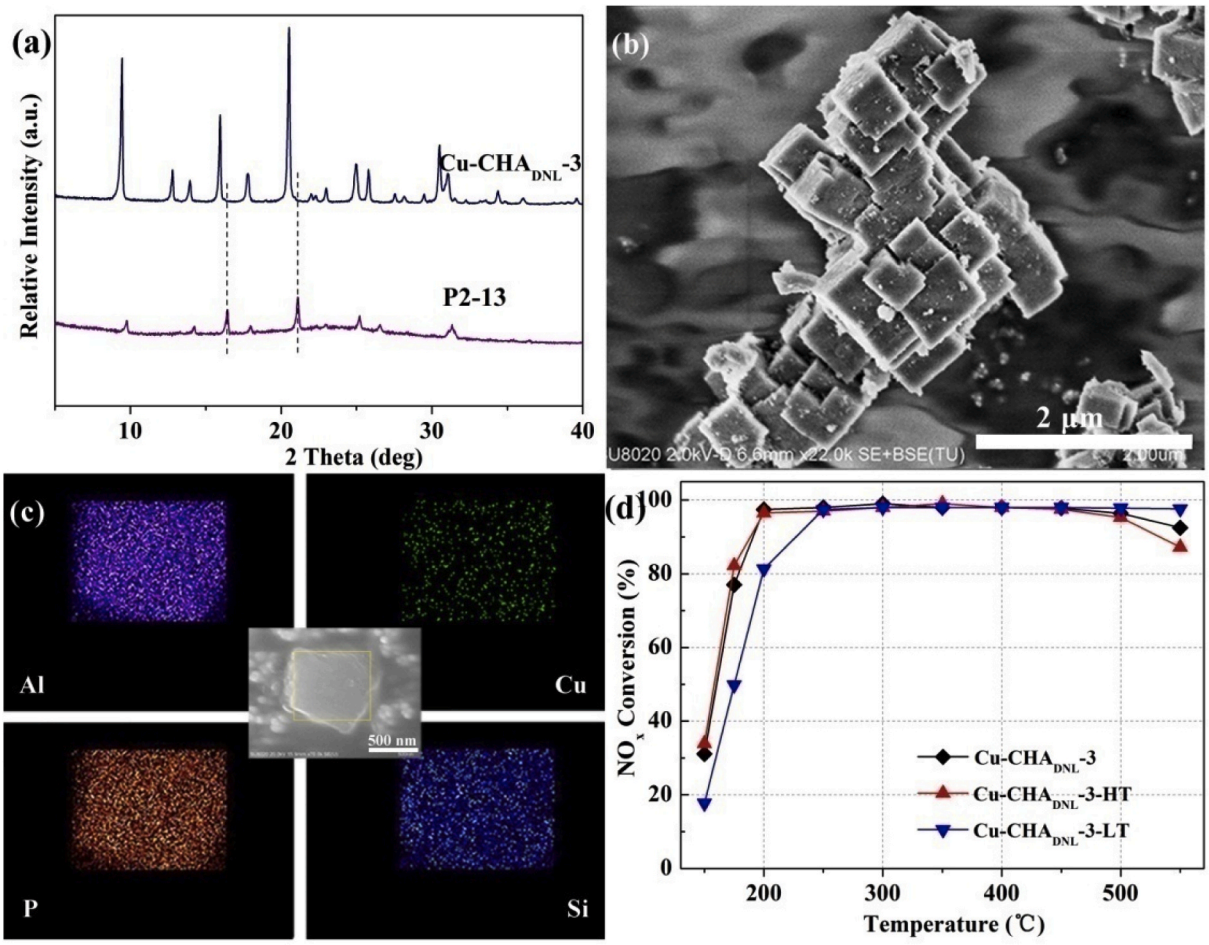

Fig. 5. (a) XRD patterns of P2-13 and Cu-CHA$_{DNL}$-3. (b) SEM image of Cu-CHA$_{DNL}$-3. (c) EDX maps (Al, Cu, P and Si) of Cu-CHA$_{DNL}$-3. (d) NO_x conversion as a function of reaction temperature over fresh (black◆), high-temperature steam treated (HT) (redig and low-temperature water soaked (LT) (blue▼) Cu-CHA$_{DNL}$-3. The peak shifts of P2-13 are labeled by dotted line. (For interpretation of the references to color in this figure legend, the reader is referred to the Web version of this article.)

to 16.3° 2θ and from 20.7° to 21.0° 2θ as compared with P1-13 (Fig. S1). This phenomenon was reported previously [39], which could be used to mark the existence of P2-13. The synthesis of Cu-CHA$_{DNL}$ was focused on the TEA-template system, and the results are listed in Table 2. The Si content of Cu-CHA$_{DNL}$ had limited increase (from 19.0 to 21.8%) as the raised silica feeding (samples Cu-CHA$_{DNL}$-1, -3, -5). In contrast, both the Si and Cu contents rose significantly as the increased P2-13 dosage (samples Cu-CHA$_{DNL}$-2, -3, -4) suggesting the participation of P2-13 in the crystallization.

The Cu-CHA$_{DNL}$ samples with different crystallization times were also investigated. As shown in Fig. S3a, new XRD peaks indexed to SAPO-34 appeared at 1 h together with the declined peak intensity belonging to P2-13. It indicates that the crystallization of Cu-CHA$_{DNL}$ happens from the very beginning accompanied with the dissolution of P2-13. The crystals grew quickly and the crystallinity reached 80% at 2 h. The XRD peaks indexed to P2-13 precursor (characteristic peak 21.0° 2θ) disappeared at 18 h indicating the crystallization completion. The liquid phases at different reaction times were also collected by centrifugal separation at 10,000 rpm and examined (Fig. S3b). It was a dark blue suspension at 1 h whose color became light at 2 h, and turned to transparent brown at 3 h. It is believed that the Cu-SSZ-13 precursor dissolves in the initial stage which participated in the crystallization of Cu-CHA$_{DNL}$ gradually. A possible crystallization process of Cu-CHA$_{DNL}$ is proposed and illustrated in Fig. 4.

In the initial stage, P2-13 dissolves and releases the CHA subunits containing Cu-TEPA in the reactant gel. The nucleation step is therefore omitted and the crystals of Cu-CHA$_{DNL}$ boom during the first 1–2 h. The crystal growth process takes nutrition concurrently from P2-13 subunits and the Si/Al/P starting reagents. This guarantees the apparent homogeneous elemental distribution of Cu-CHA$_{DNL}$ crystals. The formation of Cu-CHA$_{DNL}$ promotes the dissolution of the precursor, which further contributes to the crystallization of Cu-CHA$_{DNL}$. The precursors are completely dissolved and the crystallization is finished at around 18 h.

The Cu-CHA$_{DNL}$s synthesized with P2-13 had similar XRD patterns and SEM images to those samples synthesized with P1-13. Fig. 5 illustrates the results of Cu-CHA$_{DNL}$-3 as an example. The featured XRD peaks belonging to P2-13 couldn't be found confirming the evolution of P2-13 during the crystallization. SEM image of Cu-CHA$_{DNL}$-3 presented uniform cubic like morphology with particle size of *ca.* 600–800 nm. In order to check the homogeneity of the phase, the crystals of Cu-CHA$_{DNL}$-3 were cut into *ca.* 50 nm slices to measure EDX mapping. From Fig. 5c, it was evident that the Cu/Al/Si/P elements had uniform distributions in the crystal. The catalytic performances of fresh and aged Cu-CHA$_{DNL}$-3 are given in Fig. 5d. The similar activity and stability of Cu-CHA$_{DNL}$-3 to Cu-CHA$_{DNL}$-TEA suggested that the Si/Al ratio of the precursor has no significant influence on the properties of Cu-CHA$_{DNL}$.

Solid-state MAS NMR spectra were measured to investigate the chemical environments of Cu-CHA$_{DNL}$. The ^{31}P spectrum presented single resonance at −28 ppm assigned to phosphate groups (Fig. S4) [44]. The ^{29}Si spectrum, shown in Fig. 6a, gave the highest signal at −91 ppm attributed to Si(4Al) species. The chemical shifts at −95, −101, −105 and −110 ppm could be assigned to Si(3Al), Si(2Al), Si(1Al) and Si

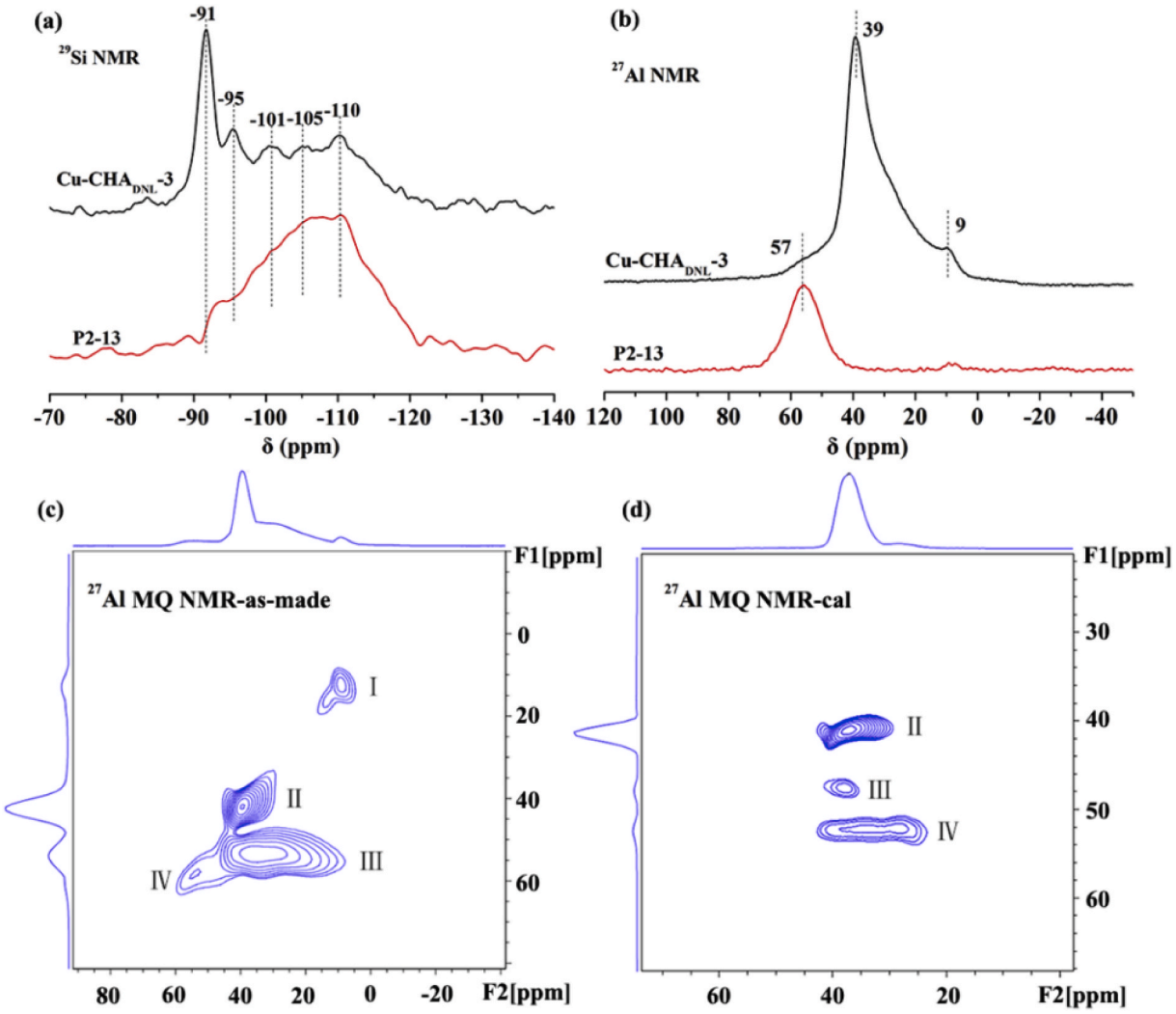

Fig. 6. (a) ^{29}Si and (b) ^{27}Al MAS NMR spectra of as-synthesized P2-13 and Cu-CHA$_{DNL}$-3.^{27}Al MQ MAS NMR spectra of (c) as-synthesized and (d) calcined Cu-CHA$_{DNL}$-3.

(0Al) species respectively [42]. Considering that Si(4Al) is the main species in conventional SAPO-34 synthesized in low-Si gel system ($SiO_2/Al_2O_3 = 0.3$) [45], it is believed that the Si(nAl) (n = 3–0) species were mainly associated with the introduced P2-13 which had only one broad ^{29}Si signal from −90 to −120 ppm (Fig. 6a). The ^{27}Al MAS NMR spectrum (Fig. 6b) showed one strong asymmetric signal at 39 ppm accompanied by two weak peaks at 9 and 57 ppm. The peak at 39 ppm is attributed to typical tetrahedral framework Al atoms of SAPO-34, while the signal at 9 ppm should be ascribed to framework Al atoms attached by additional one molecule of water or template forming pentacoordinated Al atoms [44]. The chemical shift at 57 ppm is typical tetrahedrally coordinated framework Al atoms of SSZ-13 [25]. The coexistence of various Al signals shows that Cu-CHA$_{DNL}$-3 has the microstructure of both aluminosilicate and SAPO molecular sieves. Two-dimension (2D) ^{27}Al multiple-quantum magic-angle spinning (MQ MAS) experiment was further conducted to refocus the second-order anisotropic broadening and give isotropic spectra along the F1 dimension after a shearing transformation. Four signals of 13 (I), 42 (II), 54 (III) and 57 (IV) ppm were displayed in isotropic (F1) dimension for as-synthesized Cu-CHA$_{DNL}$-3, as shown in Fig. 6c. The peak (I) can be ascribed to pentacoordinated Al which disappeared after calcination and removal of the guest molecule (Fig. 6d). The other three signals can be assigned to three types of tetrahedrally coordinated Al species. After calcination, the signals moved to 41, 48 and 52 ppm (Fig. 6d) which can be attributed to

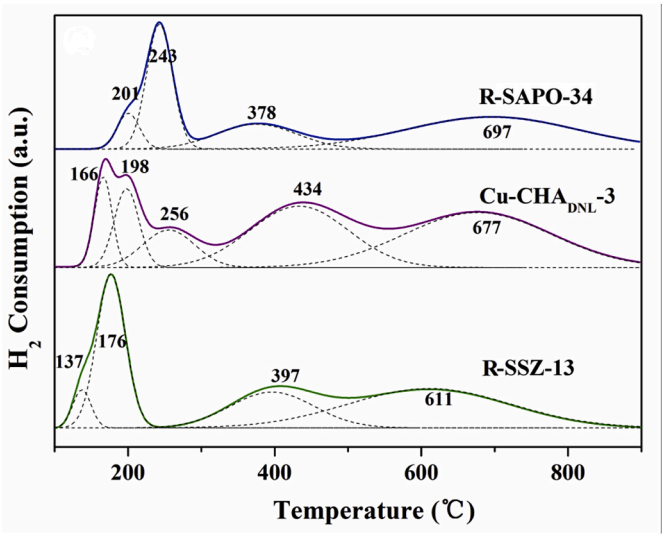

Fig. 7. H_2-TPR profiles of Cu-CHA$_{DNL}$-3, R-SSZ-13 and R-SAPO-34.

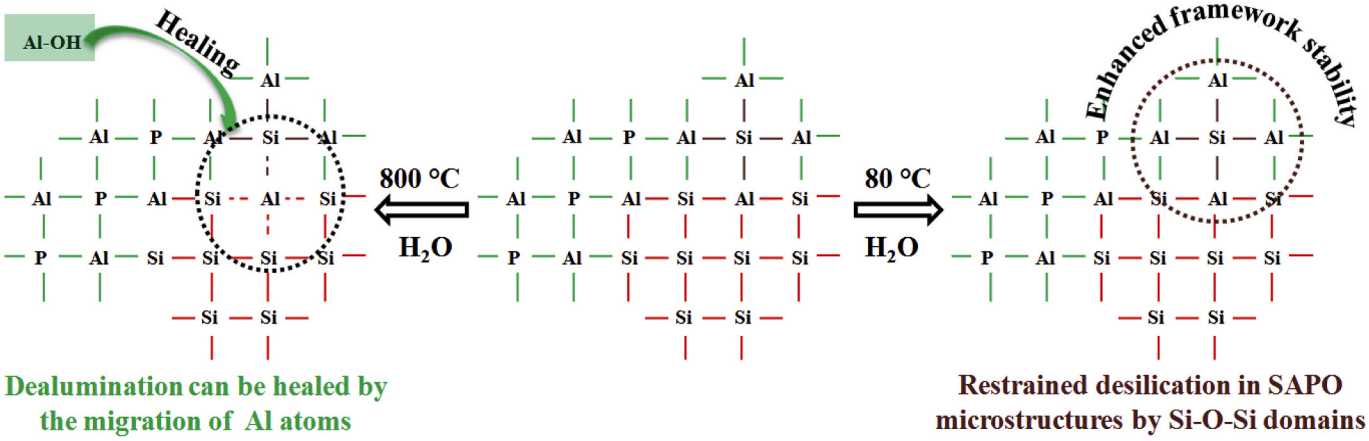

Fig. 8. Proposed mechanisms for the improvement of high and low temperature hydrothermal stabilities of the Cu-CHA$_{DNL}$ sample.

$Al(OSi)_n(OP)_{(4-n)}$ (n = 0, 1), $Al(OSi)_n(OP)_{(4-n)}$(n = 2, 3) and $Al(OSi)_4$ respectively [46]. The chemical shifts move to low field as the increased number of surrounding Si atoms. Compared to Si-rich SAPO-34, the chemical shifts of Cu-CHA$_{DNL}$-3 are at lower fields [42], which demonstrates the coexistence of aluminosilicate fragments together with SAPO framework in Cu-CHA$_{DNL}$.

H_2-TPR was conducted to probe the reducibility of the Cu species. As shown in Fig. 7, the H_2-TPR profiles of Cu-CHA$_{DNL}$-3 exhibited multiple broad peaks from *ca.* 166 to 700 °C. Based on the previous reports, these H_2 consumption peaks can be attributed to the reduction of dispersed CuO to Cu^0 (<180 °C), Cu^{2+} to Cu^+ (180–350 °C), bulk CuO to Cu^0 (350–500 °C) and Cu^+ to Cu^0 (>500 °C) respectively [18,47,48]. Interestingly, the reduction of Cu^{2+} to Cu^+ had three signals at about 198 and 256 °C, which promoted us to further investigate the status of isolated Cu^{2+} ions by EPR. The EPR profiles (Fig. S5) exhibited only one signal of $g_{\|} = 2.37$ and $A_{\|} = 139G$, showing that Cu^{2+} cations mainly locate near to the six-membered rings [49]. The reduction behavior of reference samples R-SSZ-13 and R-SAPO-34 were further measured for comparison. The reduction peaks of Cu^{2+} to Cu^+ appeared at 176 °C for R-SSZ-13 and 243 °C for R-SAPO-34 probably caused by their different framework environment. Given these results, the reduction behaviors of Cu^{2+} ions to Cu^+ for Cu-CHA$_{DNL}$-3 may be ascribed to its combination of the microstructures of Cu-SSZ-13 and Cu-SAPO-34. Moreover, DRIFT difference spectra between NH_3-saturated and NH_3-free spectra of the samples were measured to distinguish the microenvironments of Cu-CHA$_{DNL}$ (Fig. S6). All the spectra are given by subtracting the background spectra tested under the N_2 flow. According to the literatures [9,50,51], the NH_3-adsorbed DRIFTS spectra of Cu-SAPO-34 and Cu-SSZ-13 have different vibration signals in the range of 850–960 nm due to the perturbance of copper species TO_4 framework. The presence of NH_3 solvates the Cu^{2+} and thus the T-O-T vibrations preturbed by Cu^{2+} can be recovered. (the signals in the difference spectra are negative). As shown in Fig. S6, two negative bands at 911 and 957 cm^{-1} were observed for R-SSZ-13,[50] whereas for R-SAPO-34 the peaks appeared at 911 and 861 cm^{-1}. The DRIFTS spectrum of Cu-CHA$_{DNL}$ combined the features of R-SSZ-13 and R-SAPO-34 with absorption peaks at 957, 911 and 861 cm^{-1}. It confirms that the microstructures of Cu-CHA$_{DNL}$ contain the contributions of both SAPO and aluminosilicate frameworks.

3.4. Understanding the relationships between material microstructures and hydrothermal stabilities

To better understand the excellent catalytic performance and significantly improved hydrothermal stability of Cu-CHA$_{DNL}$, the fresh and aged samples were further measured by powder XRD and the patterns are shown in Fig. S7. The crystallinity of R-SSZ-13-HT after 800 °C steam aging decreased quite much, and R2-34-LT transformed to an amorphous phase after the 80 °C immersion. These results are responsible for their severely reduced NH_3-SCR activities. The well-kept crystallinity of Cu-CHA$_{DNL}$-DEA and Cu-CHA$_{DNL}$-TEA confirms again that Cu-CHA$_{DNL}$s are different from conventional SAPO-34 and SSZ-13, which can survive the harsh treatments at both high and low temperatures.

Considerable efforts have been made to understand the different hydrothermal stabilities of Cu-SSZ-13 and Cu-SAPO-34 [9,29,52–54]. Gao et al. confirmed that the difference of the hydrothermal stability of Cu-SAPO-34 and Cu-SSZ-13 catalysts might arise from the different structures and charge densities of the two zeolite frameworks [28,55]. Swang et al. pointed out that the hydrolysis of first Si–O–Al bonds for both SSZ-13 and SAPO-34 materials was qualitatively same. Divergences happened consequently due to the different preferred location of particular protons [56]. DFT calculation indicated that the dealumination process of SSZ-13 had a higher potential energy than the desilication pathway of SAPO-34 possibly due to the different microenvironments of Si–O–Al bonds [56–58]. This explains why dealumination of SSZ-13 happens only at high temperature, while desilication of SAPO-34 occurs at moisture atmosphere. As the extra-framework Al and P atoms might migrate at high temperature to heal the defects caused by desilication, SAPO-34 behaved better high-temperature hydrothermal stability than SSZ-13 [25,26].

Based on the above experimental results and analyses, it is inferred that the well fused microstructures of SSZ-13 and SAPO-34 in Cu-CHA$_{DNL}$ is the main reason for its enhanced hydrothermal stability. As illustrated in Fig. 8, the Si–O–Al bonds in SAPO zones are closely adjacent to the Si–O–Si domains of the aluminosilicate part, which may increase the potential energy of desilication for SAPO zones. The structural degradation of Cu-CHA$_{DNL}$ under moisture condition can thus be effectively restrained. On the other hand, the dealumination of aluminosilicate parts may be healed on time by their abundant Al–O–P neighbors, which can conveniently migrate to the defects at high temperature. Moreover, about 0.4–0.6% Na^+ ions of Cu-CHA$_{DNL}$ may cover the acid sites and protect the framework from H_2O attacking [20,21]. Combining all these factors, the crystallinity and the active Cu species of Cu-CHA$_{DNL}$ would be well protected under harsh hydrothermal treatment, keeping excellent NH_3-SCR and stability.

4. Conclusions

A new Cu-CHA composite with interlaced SAPO and aluminosilicate parts has been synthesized by utilizing Cu-SSZ-13 as a precursor to assist the crystallization of SAPO-34. The precursor supplied Cu source, CHA structural units and part of Si/Al source resulting in Cu-CHA$_{DNL}$ product with very high silica content, and suitable Cu and Na contents. As Cu-CHA$_{DNL}$ containing both the microstructure features of Cu-SSZ-13 and

Cu-SAPO-34, the composite Cu-CHA_{DNL} catalyst combining both the advantages of Cu-SAPO-34 and Cu-SSZ-13, behave excellent NH_3-SCR activity and robust high- and low-temperature hydrothermal stabilities. The present results suggest that Cu-CHA_{DNL} with low synthetic cost and excellent hydrothermal stability is a promising catalyst for NH_3-SCR of NO_x.

CRediT authorship contribution statement

Lijing Sun: Conceptualization, Methodology, Validation, Investigation, Formal analysis, Writing - original draft, Writing - review & editing, Resources, Visualization. **Miao Yang:** Conceptualization, Methodology, Writing - original draft, Writing - review & editing, Funding acquisition. **Lei Cao:** Formal analysis. **Yi Cao:** Formal analysis. **Shutao Xu:** Investigation. **Dali Zhu:** Investigation. **Peng Tian:** Writing - original draft, Writing - review & editing, Supervision, Project administration. **Zhongmin Liu:** Supervision, Project administration.

Declaration of competing interest

The authors declare that they have no known competing financial interests or personal relationships that could have appeared to influence the work reported in this paper.

Acknowledgements

This work was supported by the National Natural Science Foundation of China (Grant No. 21476228, 21606221, 21676262,21991090, 21991091) and the Key Research Program of Frontier Sciences, CAS (Grant No. QYZDB-SSW-JSC0 40). The authors acknowledge Dr. Wenna Zhang for the helpful discussion.

Appendix A. Supplementary data

Supplementary data to this article can be found online at .

References

[1] P. Granger, V.I. Parvulescu, Catalytic NO_x abatement systems for mobile sources: from three-way to lean burn after-treatment technologies, Chem. Rev. 111 (2011) 3155–3207.
[2] A.M. Beale, F. Gao, I. Lezcano-Gonzalez, C.H.F. Peden, J. Szanyi, Recent advances in automotive catalysis for NO_x emission control by small-pore microporous materials, Chem. Soc. Rev. 44 (2015) 7371–7405.
[3] J. Wang, H. Zhao, G. Haller, Y. Li, Recent advances in the selective catalytic reduction of NO_x with NH_3 on Cu-chabazite catalysts, Appl. Catal. B Environ. 202 (2017) 346–357.
[4] S.I. Zones, Conversion of faujasites to high-silica chabazite SSZ-13 in the presence of N,N,N-Trimethyl-1-Adamantammoniumiodide, J. Chem. Soc., Faraday Trans. 87 (1991) 3709–3716.
[5] M. Ghavipour, A.S. Mehr, Y. Wang, R.M. Behbahani, S. Hajimirzaee, K. Bahrami, Investigating the mixing sequence and the Si content in SAPO-34 synthesis for selective conversion of methanol to light olefins using morpholine &/TEAOH templates, RSC Adv. 6 (2016) 17583–17594.
[6] S. Bordiga, L. Regli, D. Cocina, C. Lamberti, M. Bjorgen, K.P. Lillerud, Assessing the acidity of high silica chabazite H-ssz-13 by FTIR using CO as molecular probe: comparison with H-SAPO-34, J. Phys. Chem. B 109 (2005) 2779–2784.
[7] N. Katada, K. Nouno, J.K. Lee, J. Shin, S.B. Hong, M. Niwa, Acidic properties of cage-based, small-pore zeolites with different framework topologies and their silicoaluminophosphate analogues, J. Phys. Chem. C 115 (2011) 22505–22513.
[8] K. Leistner, O. Mihai, K. Wijayanti, A. Kumar, K. Kamasamudram, N.W. Currier, A. Yezerets, L. Olsson, Comparison of Cu/BEA, Cu/SSZ-13 and Cu/SAPO-34 for ammonia-SCR reactions, Catal. Today 258 (2015) 49–55.
[9] D. Wang, Y. Jangjou, Y. Liu, M.K. Sharma, J. Luo, J. Li, K. Kamasamudram, W. S. Epling, A comparison of hydrothermal aging effects on NH_3-SCR of NO_x over Cu-SSZ-13 and Cu-SAPO-34 catalysts, Appl. Catal. B Environ. 165 (2015) 438–445.
[10] S.I. Zones, Zeolites SSZ-13 and its Method of Preparation, vol. 4544538, U.S. Patent, 1985.
[11] B. Chen, R. Xu, R. Zhang, N. Liu, Economical way to synthesize SSZ-13 with abundant ion-exchanged Cu^+ for an extraordinary performance in selective catalytic reduction (SCR) of NO_x by ammonia, Environ. Sci. Technol. 48 (2014) 13909–13916.
[12] G.A. Nasser, O. Muraza, T. Nishitoba, Z. Malaibari, T.K. Al-Shammari, T. Yokoi, OSDA-free chabazite (CHA) zeolite synthesized in the presence of fluoride for selective methanol-to-olefins, Microporous Mesoporous Mater. 274 (2019) 277–285.
[13] H. Imai, N. Hayashida, T. Yokoi, T. Tatsumi, Direct crystallization of CHA-type zeolite from amorphous aluminosilicate gel by seed-assisted method in the absence of organic-structure-directing agents, Microporous Mesoporous Mater. 96 (2014) 341–348.
[14] J.W. Jun, N.A. Khan, P.W. Seo, C.U. Kim, H.J. Kim, S.H. Jhung, Conversion of Y Into SSZ-13 zeolites and ethylene-to-propylene reactions over the obtained SSZ-13 zeolites, Chem. Eng. J. 303 (2016) 667–674.
[15] B. Liu, Y. Zheng, N. Hu, T. Gui, Y. Li, F. Zhang, R. Zhou, X. Chen, H. Kita, Synthesis of low-silica CHA zeolite chabazite in fluoride media without organic structural directing agents and zeolites, Microporous Mesoporous Mater. 196 (2014) 270–276.
[16] L. Ren, L. Zhu, C. Yang, Y. Chen, Q. Sun, H. Zhang, C. Li, F. Nawaz, X. Meng, F. Xiao, Designed copper-amine complex as an efficient template for one-pot synthesis of Cu-SSZ-13 zeolite with excellent activity for selective catalytic reduction of NO_x by NH_3, Chem. Commun. (J. Chem. Soc. Sect. D) 47 (2011) 9789–9791.
[17] F. Gao, N.M. Washton, Y. Wang, M. Kollár, J. Szanyi, C.H.F. Peden, Effects of Si/Al ratio on Cu/SSZ-13 NH_3-SCR catalysts: implications for the active Cu species and the roles of brønsted acidity, J. Catal. 331 (2015) 25–38.
[18] L. Xie, F. Liu, L. Ren, X. Shi, F. Xiao, H. He, Excellent performance of one-pot synthesized Cu-SSZ-13 catalyst for the selective catalytic reduction of NO_x with NH_3, Environ. Sci. Technol. 48 (2014) 566–572.
[19] A.S. Ayodhya, K.G. Narayanappa, An overview of after-treatment systems for diesel engines, Environ. Sci. Pollut. Res. 25 (2018) 35034–35047.
[20] F. Gao, Y. Wang, N.M. Washton, M. Kollar, J. Szanyi, C.H.F. Peden, Effects of alkali and alkaline earth cocations on the activity and hydrothermal stability of Cu/SSZ-13 NH_3-SCR catalysts, ACS Catal. 5 (2015) 6780–6791.
[21] Z. Zhao, R. Yu, R. Zhao, C. Shi, H. Gies, Fe Xiao, D.D. Vos, T. Yokoi, X. Bao, U. Kolb, M. Feyen, R. McGuire, S. Maurer, A. Moini, U. Müller, W. Zhang, Cu-exchanged Al-rich SSZ-13 zeolite from organotemplate-free synthesis as NH_3-SCR catalyst: effects of Na^+ ions on the activity and hydrothermal stability, Appl. Catal. B Environ. 217 (2017) 421–428.
[22] M. Yang, D. Fan, Y. Wei, P. Tian, Z. Liu, Recent progress in methanol-to-olefins (MTO) catalysts, Adv. Mater. 31 (2019), 1902181.
[23] T. Yu, D. Fan, T. Hao, J. Wang, M. Shen, W. Li, The effect of various templates on the NH_3-SCR activities over Cu/SAPO-34 catalysts, Chem. Eng. J. 243 (2014) 159–168.
[24] L. Sun, M. Yang, Y. Cao, P. Tian, P. Wu, L. Cao, S. Xu, S. Zeng, Z. Liu, A reconstruction strategy to synthesize Cu-SAPO-34 with excellent NH_3-SCR catalytic performance and hydrothermal stability, Chin. J. Catal. 41 (2020), 10. 1016.
[25] W. Su, Z. Li, Y. Peng, J. Li, Correlation of the changes in the framework and active Cu sites for typical Cu/CHA zeolites (SSZ-13 and SAPO-34) during hydrothermal aging, Phys. Chem. Chem. Phys. 17 (2015) 29142–29149.
[26] A. Buchholz, W. Wang, M. Xu, A. Arnold, M. Hunger, Thermal stability and dehydroxylation of brønsted acid sites in silicoaluminophosphates H-SAPO-11, H-SAPO-18, H-SAPO-31, and H-SAPO-34 investigated by multi-nuclear solid-state NMR spectroscopy, Microporous Mesoporous Mater. 56 (2002) 267–278.
[27] L. Wang, J.R. Gaudet, W. Li, D. Weng, Migration of Cu species in Cu/SAPO-34 during hydrothermal aging, J. Catal. 306 (2013) 68–77.
[28] F. Gao, E.D. Walter, N.M. Washton, J. Szanyi, C.H.F. Peden, Synthesis and evaluation of Cu-SAPO-34 catalysts for ammonia selective catalytic reduction. 1. Aqueous solution ion exchange, ACS Catal. 3 (2013) 2083–2093.
[29] K. Leistner, L. Olsson, Deactivation of Cu/SAPO-34 during low-temperature NH_3-SCR, Appl. Catal. B Environ. 165 (2015) 192–199.
[30] J. Fan, P. Ning, Y. Wang, Z. Song, X. Liu, H. Wang, J. Wang, L. Wang, Q. Zhang, Significant promoting effect of Ce or La on the hydrothermal stability of Cu-SAPO-34 catalyst for NH_3-SCR reaction, Chem. Eng. J. 369 (2019) 908–919.
[31] Y. Cao, L. Lan, X. Feng, Z. Yang, S. Zou, H. Xu, Z. Li, M. Gong, Y. Chen, Cerium promotion on the hydrocarbon resistance of a Cu-SAPO-34 NH_3-SCR monolith catalyst, Catal. Sci. Technol. 5 (2015) 4511–4521.
[32] F. Gao, E.D. Walter, N.M. Washton, J. Szanyi, C.H.F. Peden, Synthesis and evaluation of Cu/SAPO-34 catalysts for NH_3-SCR 2: solid-state ion exchange and one-pot synthesis, Applied Appl. Catal. B-Environ. 162 (2015) 501–514.
[33] X. Xiang, M. Yang, B. Gao, Y. Qiao, P. Tian, S. Xu, Z. Liu, Direct Cu^{2+} ion-exchanged into as-synthesized SAPO-34 and its catalytic application in the selective catalytic reduction of NO with NH_3, RSC Adv. 6 (2016) 12544–12552.
[34] R. Martinez-Franco, M. Moliner, C. Franch, A. Kustov, A. Corma, Rational direct synthesis methodology of very active and hydrothermally stable Cu-SAPO-34 molecular sieves for the SCR of NO_x, Appl. Catal. B Environ. 127 (2012) 273–280.
[35] N. Masoumifard, R. Guillet-Nicolas, F. Kleitz, Synthesis of engineered zeolitic materials: from classical zeolites to hierarchical core–shell materials, Adv. Mater. 30 (2018), 1704439.
[36] Y. Zhang, Y. Liu, L. Sun, L. Zhang, J. Xu, F. Deng, Y. Gong, Synthesis of EU-1/ZSM-48 Co-crystalline zeolites from high-silica EU-1 seeds: tailoring phase proportions and promoting long crystalline-phase stability, Chem. Eur J. 24 (2018) 6595–6605.
[37] Y. Ma, H. Zhao, C. Zhang, Y. Zhao, H. Chen, Y. Li, Enhanced hydrothermal stability of Cu-ssz-13 by compositing with Cu-SAPO-34 in selective catalytic reduction of nitrogen oxides with ammonia. Catal. Today doi.org/10.1016/j.cattod.2019.03.057.
[38] H. Zhao, Y. Zhao, Y. Ma, X. Yong, M. Wei, H. Chen, C. Zhang, Y. Li, Enhanced hydrothermal stability of a Cu-SSZ-13 catalyst for the selective reduction of NO_x by NH_3 synthesized with SAPO-34 micro-crystallite as seed, J. Catal. 377 (2019) 218–223.

[39] R. Martinez-Franco, M. Moliner, J.R. Thogersen, A. Corma, Efficient one-pot preparation of Cu-SSZ-13 materials using cooperative OSDAs for their catalytic application in the SCR of NO_x, ChemCatChem 5 (2013) 3316–3323.
[40] J.A. van Bokhoven, D.C. Koningsberger, P. Kunkeler, H. van Bekkum, A.P. M. Kentgens, Stepwise dealumination of zeolite beta at specific T-sites observed with Al-27 MAS and Al-27 MQ MAS NMR, J. Am. Chem. Soc. 122 (2000) 12842–12847.
[41] D. Wang, P. Tian, M. Yang, S. Xu, D. Fan, X. Su, Y. Yang, C. Wang, Z. Liu, Synthesis of SAPO-34 with alkanolamines as novel templates and their application for CO_2 separation, Microporous Mesoporous Mater. 194 (2014) 8–14.
[42] W. Shen, X. Li, Y. Wei, P. Tian, F. Deng, X. Han, X. Bao, A study of the acidity of SAPO-34 by solid-state NMR spectroscopy, Microporous Mesoporous Mater. 158 (2012) 19–25.
[44] J. Tan, Z. Liu, X. Bao, X. Liu, X. Han, C. He, R. Zhai, Crystallization and Si incorporation mechanisms of SAPO-34, Microporous Mesoporous Mater. 53 (2002) 97–108.
[45] B. Gao, D. Fan, L. Sun, H. An, F. Fan, S. Xu, P. Tian, Z. Liu, Insights into the aminothermal crystallization process of SAPO-34 and its comparison with hydrothermal system, Microporous Mesoporous Mater. 248 (2017) 204–213.
[46] X. Su, S. Xu, P. Tian, J. Li, A. Zheng, Q. Wang, M. Yang, Y. Wei, F. Deng, Z. Liu, Investigation of the strong bronsted acidity in a novel SAPO-type molecular sieve, DNL-6, J. Phys. Chem. C 119 (2015) 2589–2596.
[47] C. Niu, X. Shi, F. Liu, K. Liu, L. Xie, Y. You, H. He, High hydrothermal stability of Cu–SAPO-34 catalysts for the NH_3-SCR of NO_x, Chem. Eng. J. 294 (2016) 254–263.
[48] J. Wang, T. Yu, X. Wang, G. Qi, J. Xue, M. Shen, W. Li, The influence of silicon on the catalytic properties of Cu/SAPO-34 for NO_x reduction by ammonia-SCR, Applied Appl. Catal. B-Environ. 127 (2012) 137–147.
[49] J. Xue, X. Wang, G. Qi, J. Wang, M. Shen, W. Li, Characterization of copper species over Cu/SAPO-34 in selective catalytic reduction of NO_x with ammonia: relationships between active Cu sites and de-NO_x performance at low temperature, J. Catal. 297 (2013) 56–64.
[50] J.H. Kwak, H. Zhu, J.H. Lee, C.H.F. Peden, J. Szanyi, Two different cationic positions in Cu-SSZ-13? Chem. Commun. (J. Chem. Soc. Sect. D) 48 (2012) 4758–4760.
[51] L. Wang, W. Li, S.J. Schmieg, D. Weng, Role of brønsted acidity in NH_3 selective catalytic reduction reaction on Cu/SAPO-34 catalysts, J. Catal. 324 (2015) 98–106.
[52] J. Song, Y. Wang, E.D. Walter, N.M. Washton, D. Mei, L. Kovarik, M.H. Engelhard, S. Prodinger, Y. Wang, C.H.F. Peden, F. Gao, Toward rational design of Cu/SSZ-13 selective catalytic reduction catalysts: implications from atomic-level understanding of hydrothermal stability, ACS Catal. 7 (2017) 8214–8227.
[53] Y. Cao, D. Fan, L. Sun, M. Yang, L. Cao, T. Sun, S. Xu, P. Tian, Z. Liu, The self-protection effect of reactant gas on the moisture stability of Cu-SAPO-34 catalyst for NH_3-, SCR. Chem. Eng. J. 374 (2019) 832–839.
[54] A. Wang, Y. Chen, E.D. Walter, N.M. Washton, D. Mei, T. Varga, Y. Wang, J. Szanyi, Y. Wang, C.H.F. Peden, F. Gao, Unraveling the mysterious failure of Cu/SAPO-34 selective catalytic reduction catalysts, Nat. Commun. 10 (2019) 1137.
[55] F. Gao, J.H. Kwak, J. Szanyi, C.H.F. Peden, Current understanding of Cu-exchanged chabazite molecular sieves for use as commercial diesel engine DeNO_x catalysts, Top. Catal. 56 (2013) 1441–1459.
[56] T. Fjermestad, S. Svelle, O. Swang, Mechanistic comparison of the dealumination in SSZ-13 and the desilication in SAPO-34, J. Phys. Chem. C 117 (2013) 13442–13451.
[57] T. Fjermestad, S. Svelle, O. Swang, Desilication of SAPO-34: reaction mechanisms from periodic DFT calculations, J. Phys. Chem. C 119 (2015) 2073–2085.
[58] S. Malola, S. Svelle, F.L. Bleken, O. Swang, Detailed reaction paths for zeolite dealumination and desilication from density functional calculations, Angew. Chem. Int. Ed. 51 (2012) 652–655.